fluids

MDPI

Article

Passive Control of Boundary-Layer Separation on a Wind Turbine Blade Using Varying-Parameter Flow Deflector

Xin Chen, Jiaqian Qiu, Junwei Zhong *, Chaolei Zhang and Yufeng Gan

School of Mechanical and Electrical Engineering, Jiangxi University of Science and Technology, Ganzhou 341000, China; chenxinchen0324@gmail.com (X.C.); qq6515373@outlook.com (J.Q.); zhang.chaolei@xyunio.co (C.Z.); 9120200023@jxust.edu.cn (Y.G.)

* Correspondence: jwzhong0@jxust.edu.cn

Abstract

Horizontal-axis wind turbines are widely used for wind energy harvesting, but they often encounter flow separation near the blade root, leading to power loss and structural fatigue. A varying-parameter flow deflector (FD) is proposed as a passive flow control method. The FD adopts varying parameters along the blade spanwise direction to match the varying local angle of attack. Numerical simulation using the transition SST k-ω turbulence model combined with the response-surface methodology are used to investigate the effect of the varying-parameter FD on the flow structure and aerodynamic performance of the NREL Phase VI wind turbine. The results indicate that optimal performance can be achieved when the normal position of the FD increases from the blade root to the tip, and the install angle of the FD should be greater than 62° at blade section of r/R = 63.1%. Furthermore, response-surface methodology was employed to optimize the deflector parameters, with analysis of variance revealing the relative significance of geometric factors ($l_1 > l_2 > \theta_1 > \theta_2$). Compared with the original blade, the shaft torque of the controlled blade with the optimal FD is improved by 24.7% at 10 m/s.

Keywords: horizontal-axis wind turbine; flow deflector; flow control; numerical simulation; response-surface methodology

check for updates

Academic Editors: Robert Martinuzzi and Francesco De Vanna

Received: 18 September 2025
Revised: 11 October 2025
Accepted: 14 October 2025
Published: 16 October 2025

Citation: Chen, X.; Qiu, J.; Zhong, J.; Zhang, C.; Gan, Y. Passive Control of Boundary-Layer Separation on a Wind Turbine Blade Using Varying-Parameter Flow Deflector. *Fluids* **2025**, *10*, 270. https://doi.org/10.3390/fluids10100270

Copyright: © 2025 by the authors. Licensee MDPI, Basel, Switzerland. This article is an open access article distributed under the terms and conditions of the Creative Commons Attribution (CC BY) license (https://creativecommons.org/licenses/by/4.0/).

1. Introduction

Energy systems, as critical infrastructure supporting modern societal development, play an irreplaceable role in promoting economic growth and ensuring social operation. Wind energy has become the most commercially promising form of clean energy due to its wide distribution, high technological maturity, and continuously declining power generation costs. Horizontal-axis wind turbines (HAWTs) have emerged as the mainstream equipment for wind energy utilization owing to their high efficiency, mature technological pathway, and extensive application scenarios. However, HAWTs face numerous challenges during operation. With the rapid development of wind energy utilization technology, modern wind turbines exhibit a significant trend toward large scale. While this trend increases unit capacity, it also brings about complex aerodynamic issues. The blade root is prone to flow separation, resulting in significant thickening of the turbulent boundary layer. Flow separation phenomena show a markedly increasing trend particularly under complex operating conditions such as low wind speed, high turbulence intensity, and dynamic yaw. The three-dimensional flow effects generated during the operation of large-scale rotors become significantly enhanced, leading to more complex flow structures. Furthermore,

the frequency and intensity of dynamic stall phenomena increase substantially, seriously affecting aerodynamic performance. These issues not only reduce the expected annual power generation of wind farms, impacting economic benefits, but also accelerate structural fatigue damage rates and severely shorten the design life of key components.

Flow control technology has received widespread attention in recent years. The reduction in flow separation, noise, and dynamic load can be achieved by introducing specific control strategies on the wind turbine blade surface or within the flow field and thereby improving the overall performance of the wind turbine. As an approach that regulates momentum exchange between fluids to improve flow field characteristics, the core of flow control technology lies in optimizing overall flow conditions by altering local flow structures. Based on the presence or absence of auxiliary energy input, flow control technologies can be divided into two main categories: active control and passive control. Active control includes typical methods such as synthetic jets [1–3], boundary layer blowing/suction [4–7], dynamic vibrating diaphragms [8–10], and rotating cylinder devices [11–13]. These technologies can actively intervene in flow separation phenomena through external energy input, offering high control flexibility. However, complex drive systems and high energy requirements pose significant engineering challenges for practical applications. Therefore, passive flow control technologies are more suitable for flow separation control on wind turbine blades. Passive control technologies mainly rely on geometric configuration optimization for flow regulation, having the advantage of easy implementation and requiring no energy for operation. Typical passive technologies include vortex generators [14–18], leading-edge slats [19–22], trailing-edge flaps [23–25], microtabs [26,27], surface roughness strips [28–31], bio-inspired leading edges [32–35], and riblet turbulators [36–38]. These methods can effectively enhance flow stability through structural modifications and offer implementation simplicity.

Most flow control technologies are implemented near the blade leading edge, prior to the formation of the trailing-edge separation vortex or even the leading-edge separation vortex. As a typical passive flow control device, the vortex generator (VG) primarily functions by inducing specifically oriented vortex structures to enhance momentum exchange between the mainstream flow and the boundary layer flow. Scholars worldwide have systematically investigated its flow control mechanisms through experimental and numerical studies, establishing corresponding optimization design criteria. Özden et al. [39] compared experimental and numerical methods to examine single/double-row VG configurations, demonstrating that double-row VGs promote airflow reattachment at the airfoil suction-side trailing edge while significantly increasing momentum in the boundary layer. Zhu et al. [40] investigated how the installation position of the VGs affects the dynamic stall characteristics of the S809 airfoil. Their research revealed that low-profile VGs installed close to the leading edge induce premature abrupt stall and significant aerodynamic hysteresis. However, increasing VG height and utilizing double-row configurations can strengthen streamwise vortices, effectively mitigating unsteady separation and improving aerodynamic performance under dynamic conditions. Gao et al. [41] numerically investigated the flow control effectiveness of the triangular VGs with various geometric parameters, discovering a nonlinear relationship between the vortex strength and the flow control effectiveness. However, these surface-mounted structures may induce additional drag losses under non-separated flow conditions. When the boundary layer flow is attached, the disturbance effects of microstructures may reduce aerodynamic efficiency. Slats, as the most prevalent high-lift devices in aviation, are typically integrated at airfoil leading edges. Their operational principle involves accelerating high-pressure air from the pressure side to the suction side through specially designed gap structures. For horizontal-axis wind turbine applications, Mohamed et al. [42] demonstrated the superior aerodynamic and structural

performance of bio-inspired slats compared to conventional designs. Yang et al. [21] conducted numerical simulations on the S809 airfoil by combining leading-edge slats with microtabs. The results show that this method can effectively suppress flow separation and improve the aerodynamic characteristics of the S809 airfoil. Ravichandran et al. [43] examined the effectiveness of the slat extension lengths (20%, 30%, and 40% of blade span) in maximizing thrust. Though the slat shows good capability in flow control, its structural characteristic indeed increases the structural complexity and manufacturing difficulty of the blade.

Inspired by the guide vanes of wind tunnel and the deflectors of air conditioning, a novel passive technology, named the flow deflector (FD), was proposed in our previous research [44]. As shown in Figure 1, the FD consists of a set of parallel flat plates and is elevated near the leading edge of the airfoil. The incoming flow is deflected to the airfoil surface as it passes the FD. The deflected flow brings additional momentum to motivate the blade boundary layer. The flow deflection performance of the FD is closely related to its geometric parameters. For a HAWT blade, the chord length and the twist angle vary along the spanwise direction, leading to a changing local angle of attack (AoA). The FD should be carefully designed to match the varying AoA. An FD with varying parameters in the blade spanwise direction is proposed in this paper. The effect of the varying-parameter FD on the flow field and aerodynamic characteristic of the NREL Phase VI wind turbine was investigated using numerical simulation. The paper is organized as follows: Section 2 introduces the geometry of the FD and the numerical simulation model; Section 3 investigates the effect of two key structural parameters of the FD on the flow control of the rotor blade; Section 4 performs an optimization on the FD geometry using response-surface methodology; and conclusions are drawn in Section 5.

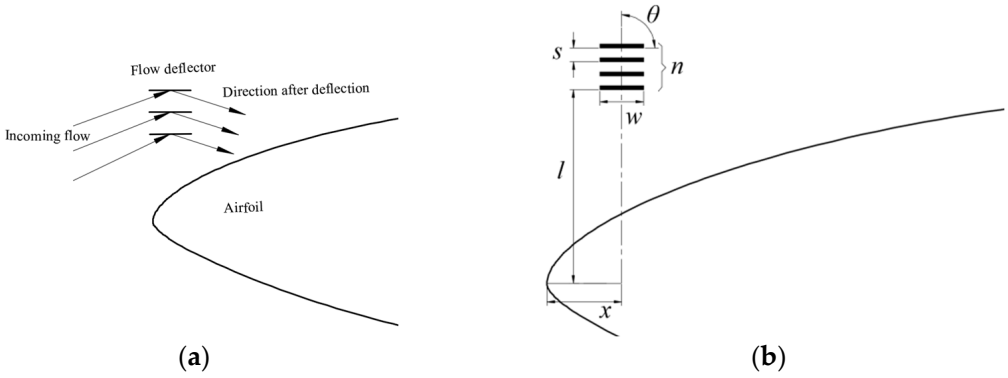


Figure 1. Schematic illustration of an airfoil with FD. (**a**) Flow deflection around the FD. (**b**) Geometric parameters of the FD.

2. Numerical Methodology

2.1. Varying-Parameter FD

The flow deflection performance of the FD is closely related to its geometric parameters. As shown in Figure 1, the geometric parameters of the FD include the following: the chordwise position, x (x is the distance from the deflector axis to the airfoil leading edge); the normal position, l (l is the distance between the bottom plate and the airfoil chord line); the installation angle, θ (θ is the angle between the deflector and its axis); the number of the deflector plates, n; the spacing between adjacent deflector plates, s; and the width of the deflector plates, w. Our previous research [44] found that the FD with $x = 0.02c$, $w = 0.02c$, and $n = 1$ obtained relatively good effectiveness in flow control. The normal position l and the installation angle θ act as threshold-sensitive parameters, which significantly influence the momentum transfer between the incoming flow and the boundary layer flow and are

critical to the effectiveness of flow control. Thus, the normal position l and the installation angle θ are determined as the two key parameters that vary along the spanwise direction of the blade. The value ranges of the two geometric parameters are determined according to the results in our previous research [44].

The NREL Phase VI rotor is a stall-regulation wind turbine. The wind turbine is a two-bladed turbine with twisted blades. The blade chord and twist distribution refer to Ref. [45]. The FD is twisted similarly to the blade, as the installation angle of the FD is defined based on the chord line of the blade section in Figure 1b. Our focus is on the wind speed of 10 m/s where the rotor starts to stall and the power begins to drop. The installation region of the FD is determined by the lift-to-drag ratio between the clean S809 airfoil and the airfoil with an FD. The results show that the FD raises the lift-to-drag ratio when the AoA is higher than 16.0° [44]. As illustrated in Figure 2, the installation region of the FD is in the range of 0.250R to 0.631R, where the local AoA is in the range of 16.5° to 22.0°. The FD is divided into ten non-equidistant sections to control its shape. The dimensionless radius of the ith section from the root to the tip is labeled as T_i.

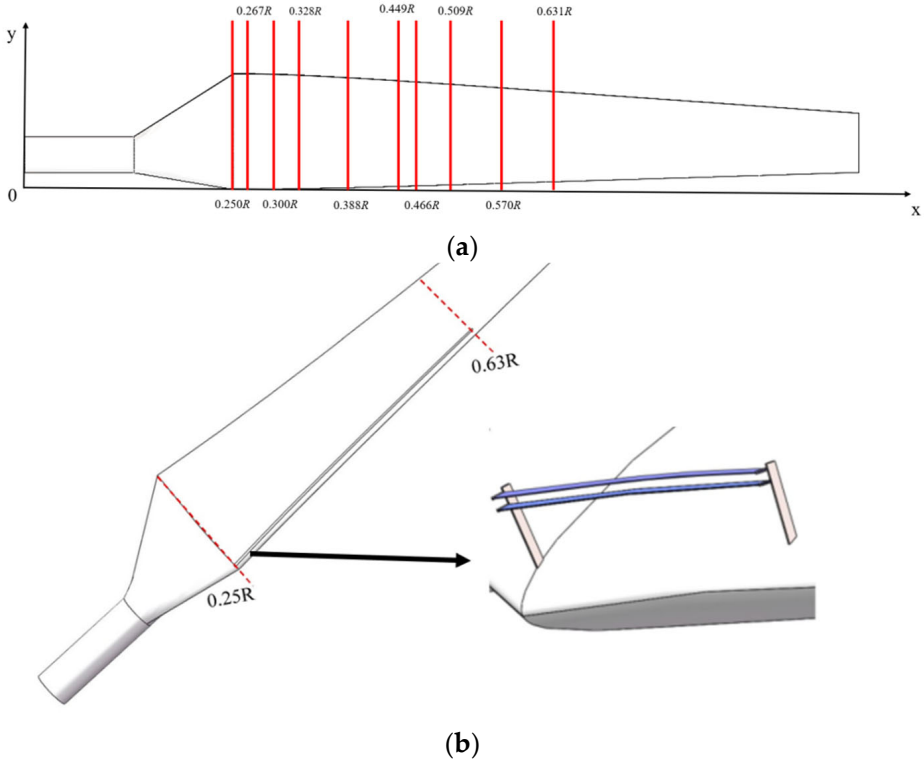


Figure 2. Schematic illustration of the blade with an FD. (**a**) Installation region of the FD. (**b**) Schematic illustration of the blade with an FD.

2.2. Boundary Conditions and Mesh Generation

The computational domain is a semi-cylinder with a radius of 3R, as shown in Figure 3. This study simulates only one blade, while the aerodynamic performance of the other blade is calculated by applying periodic boundary conditions. The computational domain is divided into two subdomains, namely the outer stationary domain and the inner rotating domain. The data exchange between the two subdomains adopts the interface technique. The inlet of the computational domain is positioned 4R upstream of the rotor and is set as the velocity inlet boundary condition. The velocity is set normal to the inlet with a turbulence intensity of 0.1%. The outlet is located 10R downstream of the rotor and is defined as the pressure outlet boundary condition. The rotating domain has a radius of

1.5R and a thickness of 0.6R. The cylindrical surface of the computational domain is set as a slip wall, while the blade surface is treated as a no-slip wall.

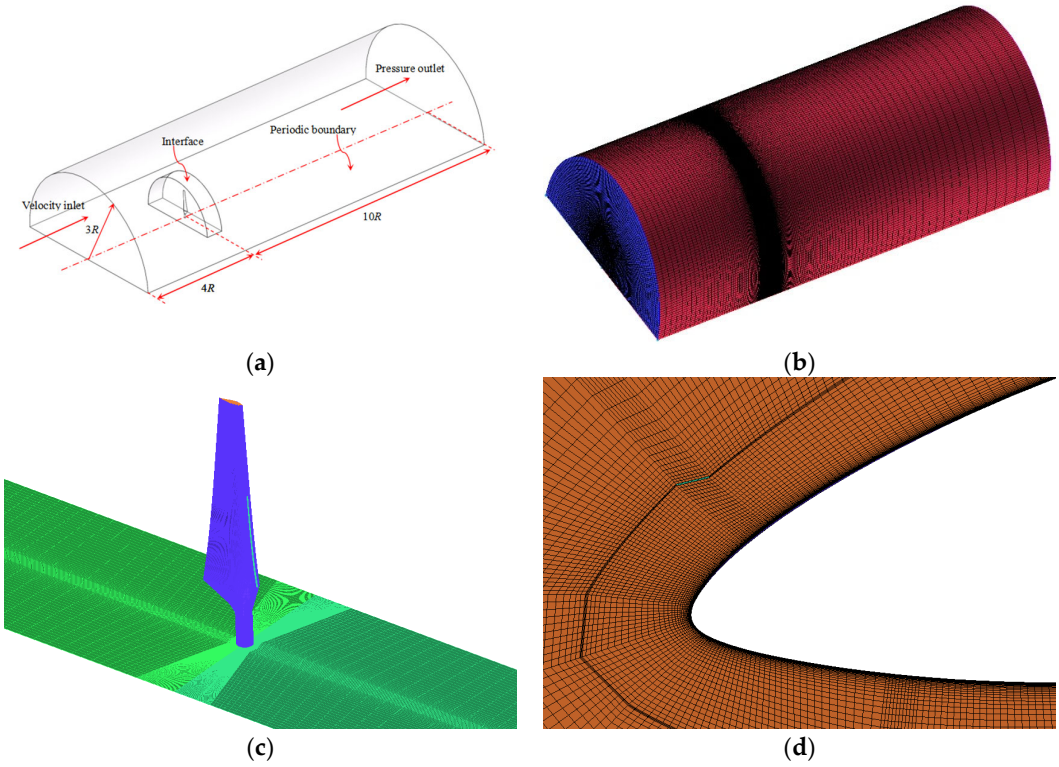


Figure 3. Schematic diagram of boundary conditions and grid generation. (**a**) Computational domain. (**b**) Grid of the stationary domain. (**c**) Grid on the blade surface. (**d**) Grid around the blade with FD.

The transition SST k-ω turbulence model is employed, with pressure–velocity coupling handled using the SIMPLEC algorithm and spatial discretization adopting the second-order upwind scheme. As illustrated in Figure 3, the computational domain is meshed in ICEM software 2022 R1 with structured grids using an O-grid topology. The grid density gradually increases from the boundaries toward the blade, and grid refinement is applied at the leading and trailing edges of the blade. The first-layer height of the blade boundary layer is set to 1×10^{-5} m to ensure $y^+ < 1$ over the majority of the blade surface.

2.3. Grid Independence Analysis and Reliability Validation

A grid independence analysis was conducted on the original blade without an FD at 10 m/s to minimize the influence of the grid on the numerical results. Four sets of grids listed in Table 1 were generated by increasing the node number in the chordwise, normal, and spanwise directions of the blade. The relationship between the grid number and blade shaft torque is illustrated in Figure 4a, which shows that the torque curve stabilizes as the number of grid cells increases. Consequently, the grid with 6.45 million cells was selected for the subsequent studies.

Table 1. Detail information about the grids.

Case	Grid 1	Grid 2	Grid 3	Grid 4
Nodes in chordwise direction	100	141	200	282
Grid size at leading edge	3.4‰c	2.4‰c	1.7‰c	1.2‰c
Nodes in normal direction	25	35	50	71
Nodes in spanwise direction	50	71	100	141
Total number of grid elements	2.6×10^6	4.38×10^6	6.45×10^6	12.2×10^6

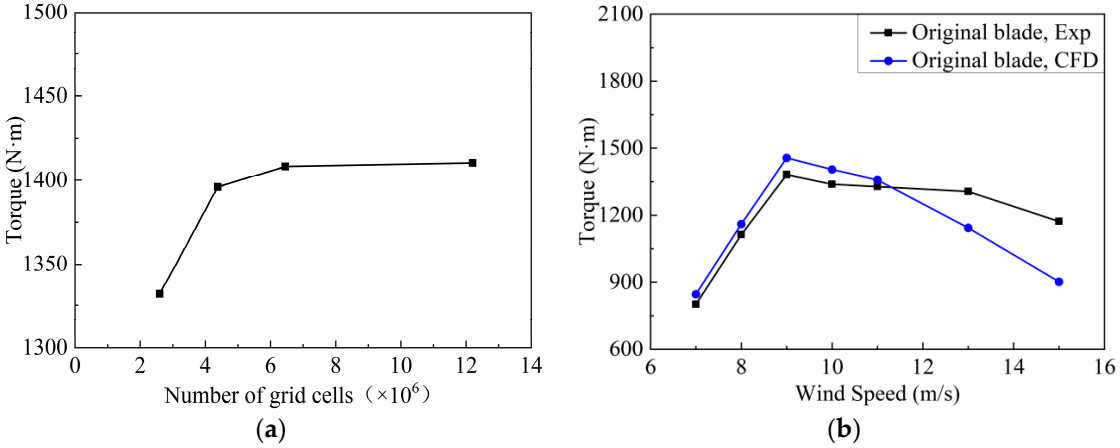


Figure 4. Grid independence analysis and reliability validation of the numerical model. (**a**) Independence analysis. (**b**) Reliability validation.

The numerical results were compared with experimental data obtained by NREL [45] to validate the reliability of the numerical model. In the study, the sequence S in the NREL test conditions was selected. The rotor adopts a yaw angle of 0°, a blade tip pitch angle of 3°, and a rotational speed of 72 rpm. As shown in Figure 4b, the simulation results exhibit good agreement with the experimental data. The maximum relative error is 5.7% at $U_\infty = 7$ m/s, confirming the reliability of the numerical model established in this study. The numerical results demonstrate relatively larger errors due to large-scale flow separation of $U_\infty \geq 13$ m/s.

3. Effects of Varying-Parameter FD on Blade Aerodynamic Performance

3.1. Influence of Normal Position

This section conducts a detailed investigation on the varying-parameter design of the normal position. The normal position varies along the spanwise direction along the blade span and is governed by the linear equation in Table 2. The range was determined by our preliminary study in Ref. [44], in which an FD having a normal position in the range of 0.04c to 0.16c was investigated. The results show that the FD deteriorates the aerodynamic performance of the airfoil when the normal position is smaller than 0.04c and performs well in the range of 0.04c to 0.12c. Moreover, the FD with a relatively close normal position performs better at large AoA, while the FD with a relatively far normal position is more suitable for small AoA. Thus, we inferred that the normal position of the FD should be gradually increased from the blade root to the tip. Nevertheless, a FD with linearly decreasing l was also designed. Other parameters of the FDs were $x = 0.02c$, $w = 0.02c$, $\theta = 90°$, and $n = 1$.

Table 2. Parameter table for different cases with varying l.

Case	l_1 (0.250R)	l_{10} (0.631R)	l_i
G1	0.105c	0.060c	$-1.18(T_i - T_{i-1})c + l_{i-1}$
G2	0.085c	0.040c	
G3	0.080c	0.125c	$1.18(T_i - T_{i-1})c + l_{i-1}$
G4	0.060c	0.105c	
G5	0.040c	0.085c	

Figure 5 presents the comparison of the shaft torques between the original blade and the blades with FDs under different wind speeds. The FDs with a linearly decreasing l,

i.e., G1 and G2, show poor effectiveness on the improvement of the shaft torque. Obvious drops of shaft torque can be observed at U_∞ = 7 m/s and 9 m/s. The drops of shaft torque at these two wind speeds are reduced for G3 and G4. Cases G3, G4, and G5 employing a linearly increasing l demonstrate superior performance on the torque improvement at $U_\infty \geq$ 10 m/s. Case G3 obtains a maximum improvement of 21.5% on the torque at 10 m/s. Case G5 obtains a maximum improvement of 31.3% on the torque at 11 m/s. However, Case G3 shows a sharp stall at U_∞ = 10 m/s and the FD has little effect on the torque at U_∞ > 10 m/s. Thus, the FD with linearly decreasing l is not recommended, while the FD with linearly increasing l still needs careful design.

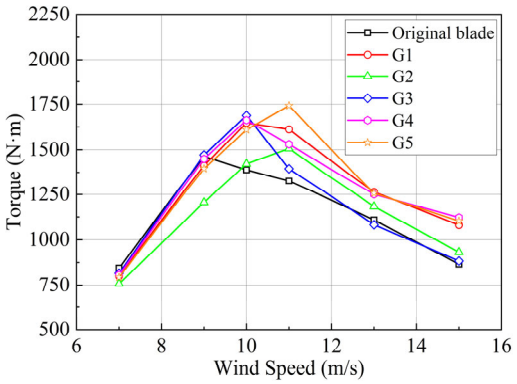


Figure 5. Torque comparison between the original blade and controlled blades with different l.

Flow structures around blade sections at r/R = 38.8% and 63.1% are compared in Figure 6. The original blade exhibits significant three-dimensional flow separation. A leading-edge separation bubble occupies the original blade suction side at r/R = 38.8% while a trailing-edge separation is observed at r/R = 63.1%. The leading-edge separation bubble is suppressed by the FD at r/R = 38.8% for G2 and G4. However, the FD blocks the flow acceleration near the blade leading-edge. As shown in Figure 6a, the negative pressure region is evidently reduced for G2 and G4. This can also be verified by the pressure coefficient distribution along the blade surface in Figure 7a. Although the peak value of the negative pressure near the leading-edge is increased by the FD, the negative pressure on most part of the suction surface is reduced. At r/R = 63.1%, the FD is too close to the blade surface for G2 and severely hinders the flow past the leading-edge, leading to stronger flow separation. By contrast, the flow separation of G4 is well controlled by the FD and the peak value of the negative pressure at the blade leading-edge is significantly raised by the FD as shown in Figure 7b.

3.2. Influence of the Installation Angle

The installation angle θ is another key parameter that influences the flow deflection performance of the FD. Five cases with different changing rules for the installation angle are listed in Table 3. The range of the installation angle was also determined by our preliminary study in Ref. [44], in which the FD with an installation angle in the range of 70° to 100° was investigated. The FD performs well when the AoA is in the range of 16° to 22°. However, the FD decreases the lift coefficient and raises the drag coefficient with the increase in installation angle when the AoA is smaller than 16°. Thus, we initially considered that the FD should adopt a gradually decreasing θ from the blade root to the tip. Nevertheless, an FD with a linearly increasing θ was also designed. Cases G6 and G7 adopt a linearly increasing θ from the blade roots to the tip, while Cases G8, G9, and G10 adopt a linearly decreasing θ. The remaining parameters of the FD are uniformly set as follows: x = 0.02c, l = 0.08c, w = 0.02c, and n = 1.

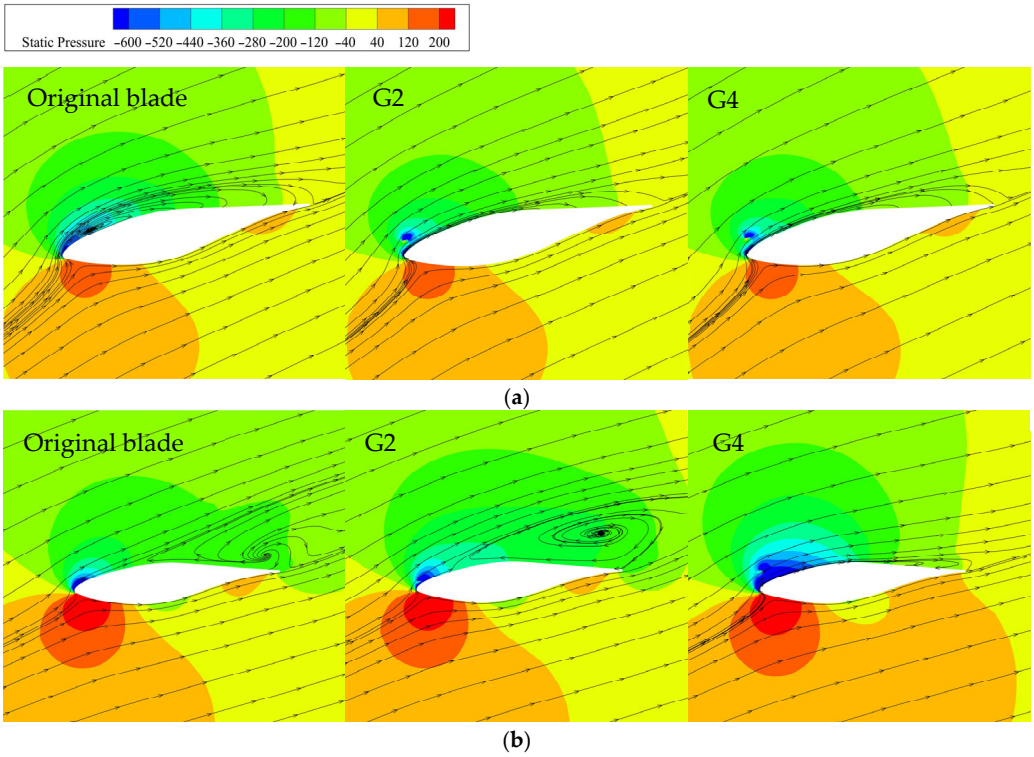


Figure 6. Pressure distribution and streamlines at two different spanwise locations. (**a**) r/R = 38.8%; (**b**) r/R = 63.1%.

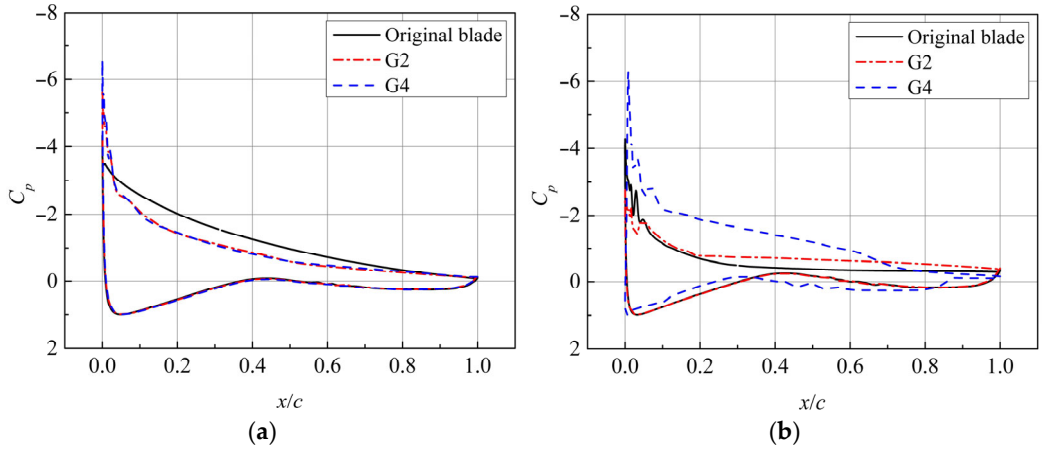


Figure 7. Pressure coefficient distribution along two different blade sections for U_∞ = 10 m/s. (**a**) r/R = 38.8%; (**b**) r/R = 63.1%.

Table 3. Parameter table for different cases with varying θ.

Case	θ_1 (0.250R)	θ_{10} (0.631R)	θ_i
G6	72°	90°	$47.37°(T_i - T_{i-1}) + \theta_{i-1}$
G7	82°	100°	
G8	100°	82°	$-47.37°(T_i - T_{i-1}) + \theta_{i-1}$
G9	90°	72°	
G10	80°	62°	

Figure 8 compares the shaft torque between the original blade and the blades with a varying-parameter FD. The torques of all cases drop slightly compared with that of the original blade at U_∞ = 7 m/s. Cases G6, G7, and G8 present more severe drops than cases G9 and G10. At U_∞ = 9 m/s, the torques of cases G9 and G10 increase slightly while the

torques of other cases are lower than that of the original blade. As the local AoA is relatively small at U_∞ = 7 m/s and 9 m/s, the FD with a large installation angle brings a barrier to the flow acceleration near the blade leading edge and additional drag. A relatively small installation angle is recommended at the FD tip for $U_\infty \leq 9$ m/s. On the other hand, a relatively small installation means that the FD becomes parallel to the local inflow, leading to a poor flow deflection performance for large local AoA. Therefore, the FD shows little effect on the torques of G9 and G10 at $U_\infty > 11$ m/s. As shown in Figure 9, the leading-edge separation bubble at r/R = 38.8% and the large-scale flow separation at r/R = 63.1% are well controlled by the FD in the case of G8. However, the FD in the case of G10 shows a negligible effect on flow separation. The other cases with relatively large installation angles obtain evident improvement on the torque at $U_\infty \geq 10$ m/s. An FD that can be adjusted according to the local AoA is deemed to perform better than a fixed FD for a wind turbine operating under different wind speeds.

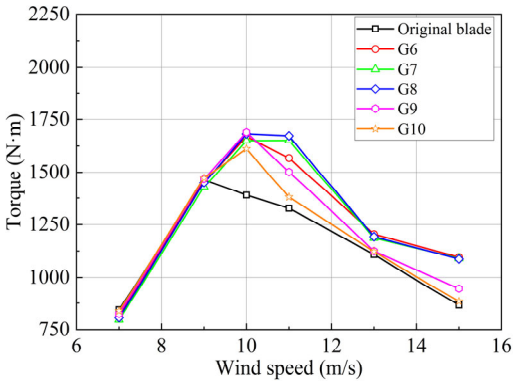


Figure 8. Torque comparison between the original blade and controlled blade with different θ.

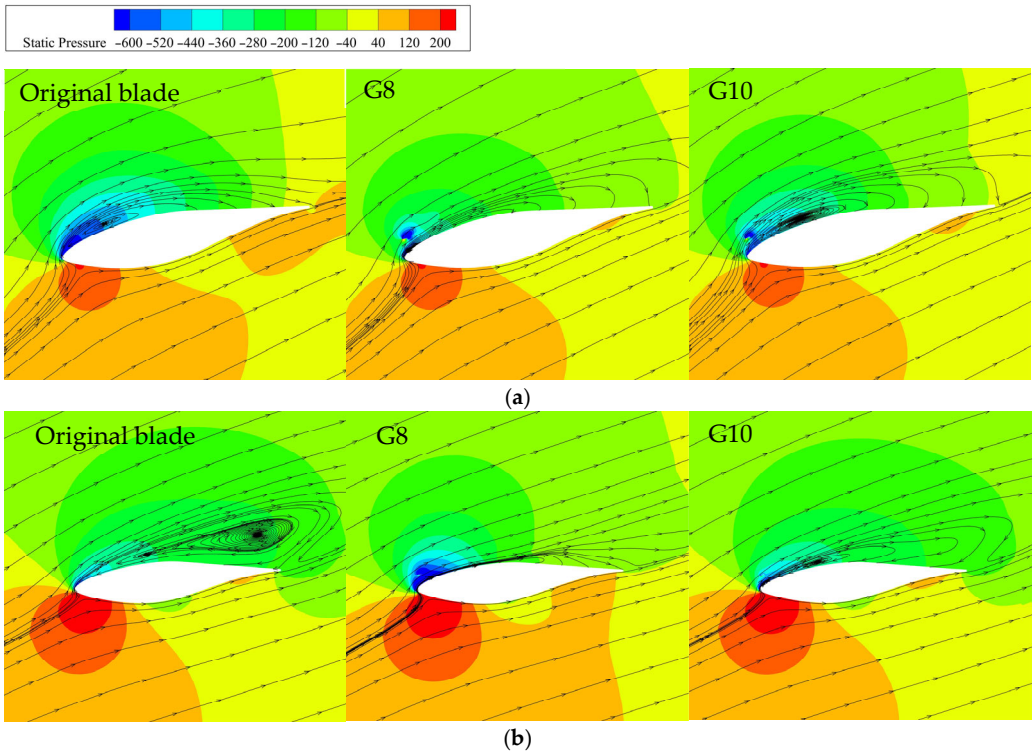


Figure 9. Pressure distribution and streamlines at two different spanwise locations for U_∞ = 11 m/s. (**a**) r/R = 38.8%; (**b**) r/R = 63.1%.

4. Optimization Design of FD Based on Response-Surface Methodology

4.1. Experiment Design and Results

Response-surface methodology was then adopted to reveal the response relationships between the geometric parameters of the FD and the blade torque at U_∞ = 10 m/s. Four key parameters, i.e., l_1 and θ_1 at the 0.250R spanwise position and l_2 and θ_2 at the 0.631R spanwise position of the blade, were selected as the design factors based on Section 3. The Box–Behnken methodology is used to design the experiment. As presented in Table 4, the four design factors were constrained within the following ranges: l_1 = (0.06~0.09) c, l_2 = (0.095~0.145) c, θ_1 = (90~100°), θ_2 = (75~85°). All 29 samples and the corresponding responses are listed in Table 5.

Table 4. Factor levels and coding.

Factor	Level		
	−1	**0**	**1**
l_1	0.06c	0.075c	0.09c
l_2	0.095c	0.120c	0.145c
θ_1	90°	95°	100°
θ_2	75°	80°	85°

Table 5. Experimental design and results.

ID	Factor A	Factor B	Factor C	Factor D	Response G
	l_1	l_2	θ_1	θ_2	Torque/(N·m)
1	0.06c	0.095c	95°	80°	1651.8
2	0.09c	0.095c	95°	80°	1664.6
3	0.06c	0.145c	95°	80°	1725.4
4	0.09c	0.145c	95°	80°	1724.4
5	0.075c	0.12c	90°	75°	1687.8
6	0.075c	0.12c	100°	75°	1687.8
7	0.075c	0.12c	90°	85°	1715.0
8	0.075c	0.12c	100°	85°	1684.7
9	0.06c	0.12c	95°	75°	1683.6
10	0.09c	0.12c	95°	75°	1716.5
11	0.06c	0.12c	95°	85°	1711.5
12	0.09c	0.12c	95°	85°	1714.8
13	0.075c	0.095c	90°	80°	1660.6
14	0.075c	0.145c	90°	80°	1720.4
15	0.075c	0.095c	100°	80°	1650.4
16	0.075c	0.145c	100°	80°	1726.8
17	0.06c	0.12c	90°	80°	1717.6
18	0.09c	0.12c	90°	80°	1716.5
19	0.06c	0.12c	100°	80°	1698.3
20	0.09c	0.12c	100°	80°	1718.6
21	0.075c	0.095c	95°	75°	1669.4
22	0.075c	0.145c	95°	75°	1729.0
23	0.075c	0.095c	95°	85°	1652.0
24	0.075c	0.145c	95°	85°	1717.1
25	0.075c	0.12c	95°	80°	1688.7
26	0.075c	0.12c	95°	80°	1688.7
27	0.075c	0.12c	95°	80°	1688.7
28	0.075c	0.12c	95°	80°	1688.7
29	0.075c	0.12c	95°	80°	1688.7

A regression analysis was conducted using the least squares method. The relationship between the response variable and the design factors was then built by quadratic polynomial fitting. The expression is formulated as follows:

$$\begin{aligned} G = {} & 1688.68 + 5.60A + 32.88B - 4.28C + 1.76D - \\ & 3.45AB + 5.36AC - 7.39AD + 4.13BC + 1.38BD - \\ & 7.57CD + 13.43A^2 - 5.55B^2 + 6.02C^2 + 4.12D^2 \end{aligned} \quad (1)$$

Variance analysis was performed to verify Equation (1). The F-value is used to measure the explanatory of the model, and the p-value is used to determine the significance of each factor. The results show the model has an F-value of 15.33 and a p-value less than 0.0001, indicating that the model is significant and highly reliable. Further analysis reveals that the significant of each factor is ranked as $A > B > C > D$ (i.e., $l_1 > l_2 > \theta_1 > \theta_2$). Additionally, the quadratic term A^2 has a significant effect on the response, indicating a quadratic relationship between independent variable A and the response. The coefficient of determination R^2 from the variance analysis was used to test the goodness-of-fit of the model. The R^2 value of Equation (1) is 0.98, indicating a good fitting performance of the regression equation. The normal plot of residuals and the relationship between the predicted torques and the actual ones are presented in Figure 10 to diagnose the goodness-of-fit of the model. Figure 10a shows that the points are close to a line, indicating the residuals of the model conform to the assumption of a normal distribution. The goodness-of-fit is also verified by the scatter diagram of the predicted torques and the actual ones. As shown in Figure 10b, the scatter points are generally located near the 45° line. The optimal parameters of the FD were finally determined as follows: l_1 = 0.061c, l_2 = 0.138c, θ_1 = 90.132°, and θ_2 = 79.834°, with a predicted shaft torque of 1729.6 N·m.

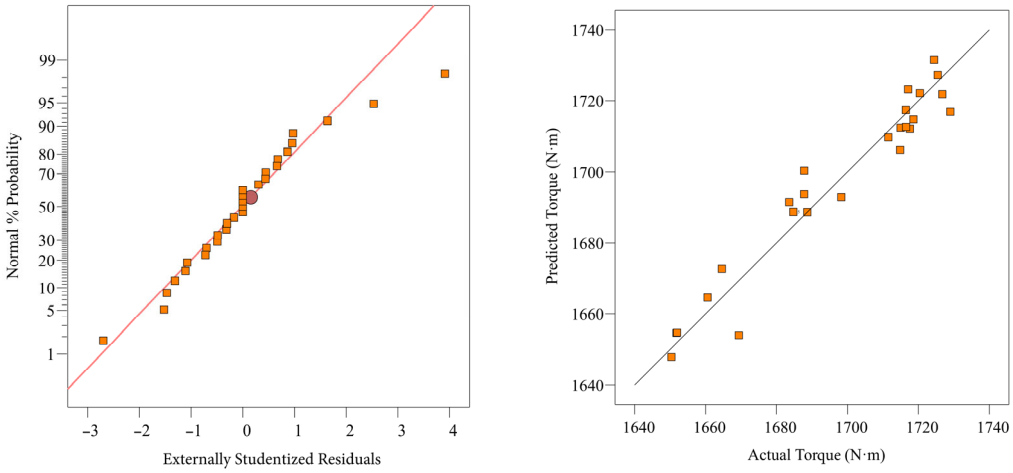


Figure 10. Diagnostics of the model. (**a**) Normal plot of residuals. (**b**) Predicted vs. actual.

4.2. Discussion

The shaft torque of the blade with an FD adopting the optimal parameters was calculated using numerical simulation. The calculated results are listed in Table 6. The shaft torque of the controlled blade at U_∞ = 10 m/s is 1731.4 N·m, showing a relative error of 0.1% compared to the RSM predicted value. The agreement between RSM predictions and numerical simulation results further validates the reliability of the established response-surface model. Compared to the original blade, the shaft torque of the controlled blade drops slightly at U_∞ = 7 m/s, while achieving a 24.6% increment at U_∞ = 10 m/s.

Table 6. Shaft torque of the blade with FD adopting the optimal parameters.

Wind Speed (m/s)	Shaft Torque (N·m)		Relative Increment (%)
	Original Blade	Controlled Blade	
7	843.8	835.2	−1.0
9	1463.2	1492.0	2.0
10	1389.2	1731.4	24.6
11	1326.6	1499.2	13.0
15	886.0	1035.8	16.9

Figure 11 shows the isosurface of the Q-criterion around the blade at 10 m/s. The value of the Q-criterion is 100 and the isosurface is colored by the turbulent kinetic energy. The original blade is surrounded by a large-scale separated vortex from the root to the mid-span. The FD effectively suppresses flow separation. The vortex at the mid-span of the controlled blade is nearly eliminated by the FD. Figure 12 presents a comparative analysis on the sectional pressure distributions between the original blade and the controlled blade at different spanwise positions at U_∞ = 10 m/s. The results demonstrate that the FD significantly influences the pressure distribution in the mid-span regions (r/R = 46.6% and 63.3%). These modifications are particularly effective in delaying flow separation onset. Moreover, the negative pressure at the leading edge of the r/R = 80% section shows a slight increase due to the three-dimensional effects.

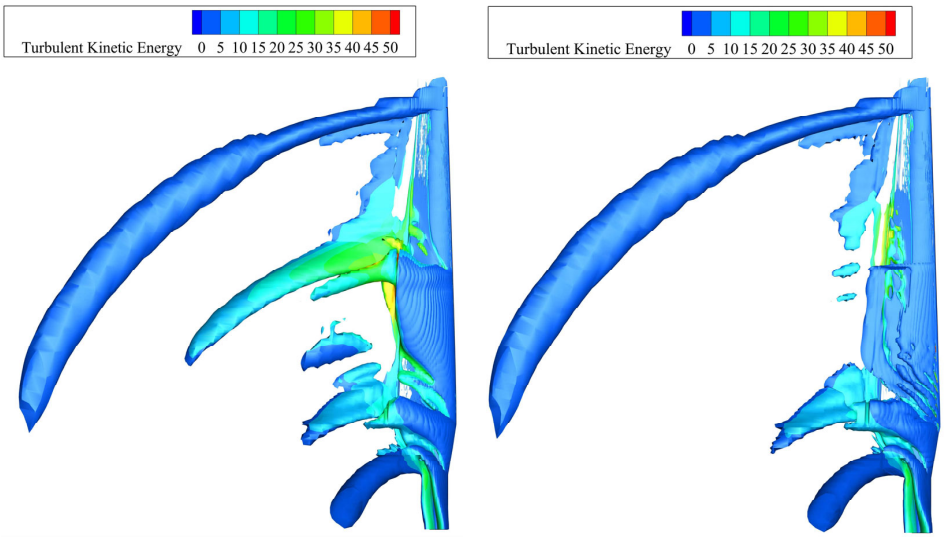


Figure 11. Isosurface of Q-criterion (Q = 100) colored by turbulent kinetic energy at 10 m/s. (**a**) Original blade. (**b**) Controlled blade.

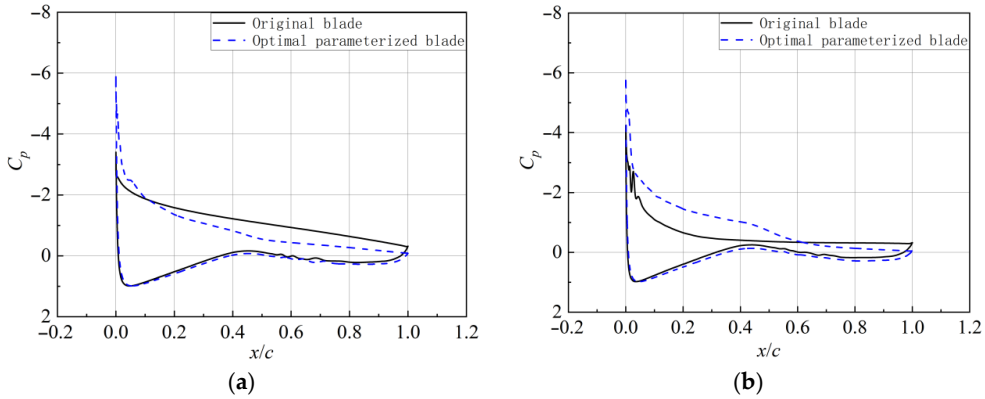


Figure 12. *Cont.*

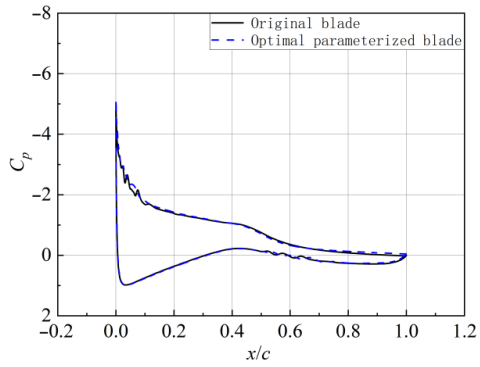


Figure 12. Pressure coefficient distribution along blade sections at 10 m/s. (**a**) r/R = 46.6%; (**b**) r/R = 63.3%; (**c**) r/R = 80%.

5. Conclusions

This study investigates the flow control effects of a varying-parameter FD on the NREL Phase VI wind turbine using numerical simulation and response-surface methodology. The results provide a theoretical foundation for engineering applications. The main conclusions are as follows:

(1) The varying-parameter FD installed on the blade leading-edge effectively enhances the aerodynamic performance of the NREL Phase VI wind turbine at $U_\infty \geq 10$ m/s. At $U_\infty \leq 9$ m/s, the FD introduces additional flow losses due to the small local angle of attack, resulting in a slight reduction in torque.

(2) The normal position l and the installation angle θ of the FD play critical roles in the improvement of the blade's aerodynamic performance. For the normal position l, a linearly increasing design from the blade root to the tip is recommended. A maximum improvement of 21.5% on the torque at 10 m/s was obtained by Case G3 which adopts $l_1 = 0.080c$ at r/R = 25.0% and $l_{10} = 0.125c$ at r/R = 63.1%. For the installation angle θ, a value bigger than 62° is suggested for the blade section at r/R = 63.1%.

(3) Within the selected parameter ranges, the FD parameters were optimized using RSM. Analysis of variance quantifies the influence of each geometric parameter on blade shaft torque, revealing the following order of significance: $l_1 > l_2 > \theta_1 > \theta_2$. The optimal parameters were determined as follows: $l_1 = 0.061c$, $l_2 = 0.138c$, $\theta_1 = 90.132°$, and $\theta_2 = 79.834°$. At 10 m/s wind speed, the aerodynamic performance of the wind turbine is further improved by the optimal FD, with a 24.7% increase in blade torque.

Author Contributions: Conceptualization, J.Z.; methodology, X.C. and J.Q.; software, X.C.; validation, X.C.; formal analysis, X.C. and J.Q.; investigation, X.C.; resources, X.C.; data curation, J.Q.; writing—original draft preparation, X.C.; writing—review and editing, J.Z.; visualization, J.Q.; supervision, Y.G.; project administration, C.Z.; funding acquisition, J.Z., C.Z., and Y.G. All authors have read and agreed to the published version of the manuscript.

Funding: This research was funded by the Natural Science Foundation of Jiangxi Province, grant numbers 20224BAB214061 and 20242BAB20217, and the National Natural Science Foundation of China, grant number 52166002.

Institutional Review Board Statement: Not applicable.

Informed Consent Statement: Not applicable.

Data Availability Statement: The data are available from the corresponding author on reasonable request.

Conflicts of Interest: The authors declare no conflicts of interest. The funders had no role in the design of the study; in the collection, analysis, or interpretation of data; in the writing of the manuscript; or in the decision to publish the results.

Abbreviations

The following abbreviations are used in this manuscript:

AoA	Angle of attack
FD	Flow deflector
HAWT	Horizontal-axis wind turbine
VG	Vortex generator

References

1. Lahoz, M.; Nabhani, A.; Saemian, M.; Bergada, J.M. Wind turbine enhancement via active flow control implementation. *Appl. Sci.* **2024**, *14*, 11404. [CrossRef]
2. Li, L.; Xia, H.S.; Du, B.X.; Bai, X.L.; Pan, J. Study on effect of synthetic jet on vortex-induced motion of spar-type floating offshore wind turbines. *Acta Energiae Solaris Sin.* **2024**, *45*, 459–466. (In Chinese)
3. Li, D.; Li, C. Numerical analysis of aerodynamic characteristic for vertical axis wind turbine of trailing edge jet. *J. Harbin Inst. Technol.* **2022**, *54*, 58–64. (In Chinese)
4. Chen, W.S.; Sun, X.J. A comparative study of the influences of leading-edge suction and blowing on the aerodynamic performance of a horizontal-axis wind turbine. *J. Energy Eng.* **2023**, *149*, 04022051.
5. Liu, Q.; Miao, W.; Bashir, M.; Xu, Z.; Yu, N.; Luo, S.; Li, C. Aerodynamic and aeroacoustics performance assessment of a vertical axis wind turbine by synergistic effect of blowing and suction. *Energy Convers. Manag.* **2022**, *271*, 116289. [CrossRef]
6. Wang, G.; Lewalle, J.; Glauser, M.; Walczak, J. Investigation of the benefits of unsteady blowing actuation on a 2D wind turbine blade. *J. Turbul.* **2013**, *14*, 165–189. [CrossRef]
7. James, S.E.; Suryan, A.; Sebastian, J.J.; Mohan, A.; Kim, H.D. Comparative study of boundary layer control around an ordinary airfoil and a high lift airfoil with secondary blowing. *Comput. Fluids* **2018**, *164*, 50–63. [CrossRef]
8. Lee, T.; Gerontakos, P. Investigation of flow over an oscillating airfoil. *J. Fluid Mech.* **2004**, *512*, 313–341. [CrossRef]
9. Di, G.; Wu, Z.; Huang, D. The research on active flow control method with vibration diaphragm on a NACA0012 airfoil at different stalled angles of attack. *Aerosp. Sci. Technol.* **2017**, *69*, 76–86. [CrossRef]
10. Kang, W.; Lei, P.; Zhang, J.; Xu, M. Effects of local oscillation of airfoil surface on lift enhancement at low Reynolds number. *J. Fluids Struct.* **2015**, *57*, 49–65. [CrossRef]
11. Al-Garni, A.Z.; Al-Garni, A.M.; Ahmed, S.A.; Sahin, A.Z. Flow control for an airfoil with leading-edge rotation: An experimental study. *J. Aircr.* **2000**, *37*, 617–622. [CrossRef]
12. Lee, T.; Mokhtarian, F.; Kafyeke, F. Flow past an airfoil with a leading-edge rotation cylinder. *J. Aircr.* **2002**, *39*, 1079–1084. [CrossRef]
13. Lu, Z.Y. Separation control for a strake-wing by rotating cone placed near the leading edge. In Proceedings of the Reno: 38th Aerospace Sciences Meeting and Exhibit, Reno, NV, USA, 10–13 January 2000.
14. Heejeon, I.; Seongkeon, K. Investigation of effective design and application of vortex generators for the wind turbine blades. *J. Mech. Sci. Technol.* **2025**, *39*, 671–685. [CrossRef]
15. Singh1, J.; Kumar, A.; Singh, A.P.; Singh, O. Study of vortex dynamics in a solar tower vortex generator. *Energy Convers. Manag.* **2024**, *316*, 118824. [CrossRef]
16. Palanivel, H.; Mukherjee, R. Airfoil-shaped vortex generators for separation control and drag reduction on wind turbine blades. *Acta Mech.* **2024**, *235*, 7765–7787. [CrossRef]
17. Kayastha, A.; Neopane, P.H.; Dahlhaug, G.O. A numerical study on the effect of spanwise installation of vortex generators on Francis runner blades. *IOP Conf. Ser. Earth Environ. Sci.* **2024**, *1385*, 012015. [CrossRef]
18. Schaffarczyk, A.P.; Lobo, B.A.; Balaresque, N.; Kremer, V.; Suhr, J.; Wang, Z. Development and Measurement of a Very Thick Aerodynamic Profile for Wind Turbine Blades. *Wind* **2024**, *4*, 190–207. [CrossRef]
19. Monat, S.; Kor, A.; Seifert, A.; Stalnov, O. Experimental investigation of suction and oscillatory blowing as an alternative for a leading edge slat. *Aerosp. Sci. Technol.* **2024**, *151*, 109227. [CrossRef]
20. Zhang, R.; Li, D.; Chang, H.; Wei, X.; Tan, Y. Optimal design of multi-objective aerodynamic performance of leading edge slat. *J. Aerosp. Power* **2025**, *40*, 191–203. (In Chinese)
21. Li, Y.; Wang, H.P.; Wu, Z.G. Aerodynamic characteristic of wind turbine with the leading-edge slat and Microtab. *Sustain. Energy Technol. Assess.* **2022**, *52*, 101957.

22. Zaki, A.; Abdelrahman, M.; Abdellatif, O. Effects of leading-edge slat on the aerodynamic performance of low Reynolds number horizontal axis wind turbine. *Energy* **2022**, *239*, 122338. [CrossRef]
23. Yin, R.; Xie, B.J.; Yao, J. Numerical and experimental study of the effect of an innovative trailing-edge flap on the aerodynamic performance of small-scale horizontal-axis wind turbines. *Wind Eng.* **2024**, *48*, 999–1011. [CrossRef]
24. Yin, R.; Xie, B.J.; Yao, J. Effects of the morphed trailing-edge flap parameters on the aerodynamic performance of NREL Phase II wind turbine. *Wind Eng.* **2024**, *48*, 784–803. [CrossRef]
25. Qian, Y.R.; Zhang, Y.Q.; Sun, Y.K. Numerical investigations of the flow control effect on a thick wind turbine airfoil using deformable trailing edge flaps. *Energy* **2023**, *265*, 126327. [CrossRef]
26. Oerlemans, S.; Migliore, P. Wind tunnel aeroacoustic tests of six airfoils for use on small wind turbines. *J. Sol. Energy Eng.* **2004**, *126*, 974–985. [CrossRef]
27. Wu, Z.; Yang, Y.; Liu, M.; Zhang, K. Numerical study on flow characteristics of airfoil with bionic micro-grooves. *J. Braz. Soc. Mech. Sci. Eng.* **2022**, *44*, 505. [CrossRef]
28. Simens, M.; Gungor, A. The Effect of Surface Roughness on Laminar Separated Boundary Layers. *J. Turbomach.* **2014**, *136*, 031014. [CrossRef]
29. Al Bari, M.A.; Mashud, M.; Ali, H. Role of partially bumpy surface to control the flow separation of an airfoil. *J. Eng. Appl. Sci.* **2012**, *7*, 584–587.
30. Fan, S.; Zhan, J.; Hu, J.; Liang, P.; Feng, X.; Dai, L. Influence of distributed leading edge roughness on aerodynamic performance of wind foil. *Acta Energiae Solaris Sin.* **2023**, *44*, 325–330. (In Chinese)
31. Bao, N.; Ni, W. Influence of additional rough strap of wind turbine airfoil leading edge surface on aerodynamic performance. *Acta Energiae Solaris Sin.* **2008**, *29*, 1465–1470. (In Chinese)
32. Hansen, K.; Rostamzadeh, N.; Kelso, R.M.; Dally, B.B. Evolution of the streamwise vortices generated between leading edge tubercles. *J. Fluid Mech.* **2016**, *788*, 730–766. [CrossRef]
33. Wei, X.; Li, D.; Chang, H.; Zhang, R.; Yang, Q.; Wang, H. Mechanism of bionic leading-edge protuberances on the aerodynamic performance of horizontal axis wind turbine. *J. Mech. Sci. Technol.* **2024**, *38*, 6607–6620. [CrossRef]
34. Skillen, A.; Revell, A.; Pinelli, A.; Piomelli, U.; Favier, J. Flow over a wing with leading-edge undulations. *AIAA J.* **2015**, *53*, 464–472. [CrossRef]
35. Zhao, M.; Zhang, M.M.; Xu, J.Z. Numerical simulation of flow characteristics behind the aerodynamic performances on an airfoil with leading edge protuberances. *Eng. Appl. Comput. Fluid Mech.* **2017**, *11*, 193–209. [CrossRef]
36. Zhao, M.; Lan, X.; Hou, B.; Liu, Y. Numerical simulation of drag reduction on wind turbine airfoil surfaces using convex hull structrues. *Acta Energiae Solaris Sin.* **2024**, *45*, 574–585. (In Chinese)
37. Sareen, A.; Deters, R.; Henry, S.; Selig, M.S. Drag reduction using riblet film applied to airfoils for wind turbines. *J. Sol. Energy Eng.* **2014**, *136*, 021007. [CrossRef]
38. Chamorro, L.; Arndt, R.; Sotiropoulos, F. Drag reduction of large wind turbine blades through riblets: Evaluation of riblet geometry and application strategies. *Renew. Energy* **2013**, *50*, 1095–1105. [CrossRef]
39. Özden, M.; Genc, M.; Koca, K. Passive flow control application using single and double vortex generator on S809 wind turbine airfoil. *Energies* **2023**, *16*, 5339. [CrossRef]
40. Zhu, C.; Feng, Y.; Shen, X.; Dang, Z.; Chen, J.; Qiu, Y.; Feng, Y.; Wang, T. Effects of the height and chordwise installation of the vane-type vortex generators on the unsteady aerodynamics of a wind turbine airfoil undergoing dynamic stall. *Energy* **2023**, *266*, 126418. [CrossRef]
41. Gao, L.; Zhang, H.; Liu, Y.; Han, S. Effects of vortex generators on a blunt trailing-edge airfoil for wind turbines. *Renew. Energy* **2015**, *76*, 303–311. [CrossRef]
42. Mohamed, M.; Reddy, K.; Vishnu, S. Bio-inspired optimization of leading-edge slat. *Aircr. Eng. Aerosp. Technol.* **2022**, *95*, 725–733. [CrossRef]
43. Ravichandran, K.; Chopra, I. Open-loop control of performance and vibratory loads using leading-edge slats. *J. Am. Helicopter Soc.* **2016**, *61*, 1–9. [CrossRef]
44. Zhao, L.; Zhong, J.W.; Tang, J.; Liu, H. Effect of Flow Deflector on the aerodynamic performance of the S809 airfoil. *J. Phys. Conf. Ser.* **2024**, *2860*, 012020. [CrossRef]
45. Hand, M.; Simms, D.; Fingersh, L.; Jager, D.; Cotrell, J.; Schreck, S.; Larwood, S. *Unsteady Aerodynamics Experiment Phase VI: Wind Tunnel Test Configurations and Available Data Campaigns*; National Renewable Energy Lab: Golden, CO, USA, 2001.

Disclaimer/Publisher's Note: The statements, opinions and data contained in all publications are solely those of the individual author(s) and contributor(s) and not of MDPI and/or the editor(s). MDPI and/or the editor(s) disclaim responsibility for any injury to people or property resulting from any ideas, methods, instructions or products referred to in the content.